ADVANCED MATERIALS

Supporting Information

for *Adv. Mater.,* DOI: 10.1002/adma.202105485

Realization of an Artificial Visual Nervous System using an Integrated Optoelectronic Device Array

*Tae-Ju Lee, Kwang-Ro Yun, Su-Kyung Kim, Jong-Ho Kim, Junyoung Jin, Kee-Baek Sim, Da-Hoon Lee, Gyu Weon Hwang, and Tae-Yeon Seong**

Supporting Information

Realization of an Artificial Visual Nervous System using an Integrated Optoelectronic Device Array

*Tae-Ju Lee, Kwang-Ro Yun, Su-Kyung Kim, Jong-Ho Kim, Junyoung Jin, Kee-Baek Sim, Da-Hoon Lee, Gyu Weon Hwang, and Tae-Yeon Seong**

T.-J. Lee, D.-H. Lee, Prof. T.-Y. Seong
Department of Nanophotonics
Korea University
145 Anam-ro, Seongbuk-gu, Seoul 02841, Republic of Korea
E-mail: tyseong@korea.ac.kr

K.-R. Yoon, S.-K. Kim, J.-H. Kim, K.-B. Sim, Prof. T.-Y. Seong
Department of Materials Science and Engineering
Korea University
145 Anam-ro, Seongbuk-gu, Seoul 02841, Republic of Korea
E-mail: tyseong@korea.ac.kr

J. Jin, Dr. G. W. Hwang
Center for Neuromorphic Engineering
Korea Institute of Science and Technology (KIST)
5, Hwarang-ro 14-gil, Seongbuk-gu, Seoul 02792, Republic of Korea

Keywords: sensory adaptation, artificial synapses, perovskite patterning, polymer electrolytes

Note S1. Desensitization mechanism of mechanotransducer channel in biological sensory neurons.

The mechanism of desensitization that underlies physiological adaptation process can be described for the time-dependent mechanosensitive channel gating, as shown in Figure S23. The adaptation of mechanotransducer channel is related to the relaxation of tension by the interaction between tension-sensing element and hinge of the ion-channel gate. Precisely, the initial state of mechanotransducer channel is closed and blocks the flow of ion migration. However, external stimuli can trigger tension-sensing element, which tempts the mechanotransducer channel to open and makes it favorable for the flow of ions, and may lead to peak response. As the stimulus is maintained, the relaxtion of tension by the free energy reduction of the mechanotransducer channel may result in a decrease in ion flux, which may no longer sustain channel activity. Finally, mechanotransducer channel either inactivates or adapts.

Note S2. Calculations that derive t_{tr} by differentiating Equation (6).

In the EPSC responses of a DAVAN device, as shown in Figure 4d, facilitation and inhibition behabiours were observed. Assuming that the $EPSC_{peak}$ curves were fitted by composition of two diffrent exponential, growth and decay functions. Moreover, to further understand the dominance of sensitization and habituation, t_{tr} was calcuated by differentiating Equation (6) from t as following equation:

$$\frac{d\mathrm{EPSC_{peak}}}{dt} = \frac{A}{\tau_{se}\tau_{ha}}\left[(\tau_{se} + \tau_{ha})e^{-t/\tau_{se}} - \tau_{se}\right]e^{-t/\tau_{ha}} \quad \text{(S1)}$$

From the above equation, t_{tr} can be derived when $\frac{d\mathrm{EPSC_{peak}}}{dt} = 0$, and determined by following equation:

$$t_{tr} = \ln\left(1 + \frac{\tau_{ha}}{\tau_{se}}\right)^{\tau_{se}} \quad \text{(S2)}$$

3D plot of t_{tr} and associated fitting surface using Equation (8) are summarized as a function of τ_{se} and τ_{ha}, as shown in Figure S28b.

Note S3. Formation of hydrophilic/hydrophobic patterned surfaces with insertion of SiO_x film as an auxiliary layer.

The surface energy can be modulated through tuning the composition of functional groups of SAMs on the surfaces of various substrate such as metals and oxides. In general, functional groups of the SAMs are attached to the surfaces to be paired appropriately, following the "hard-soft" rules associated with the polarizability of the participants. Especially, silane groups ($SiCl_3$) of the ODTS and OTS can react with hydroxyl-rich oxide surfaces such as glass, SiO_x film, AlO_x film, and nylon polymer. However, they are unpolarizable with metal surfaces such as Au film, Ag film, and Pt film (see Figure S3 and Table S1). For the formation of uniform hydrophilic/hydrophobic patterned surfaces, an hydroxyl-rich SiO_x film was inserted on the subatrate in process prior to SAM coating.

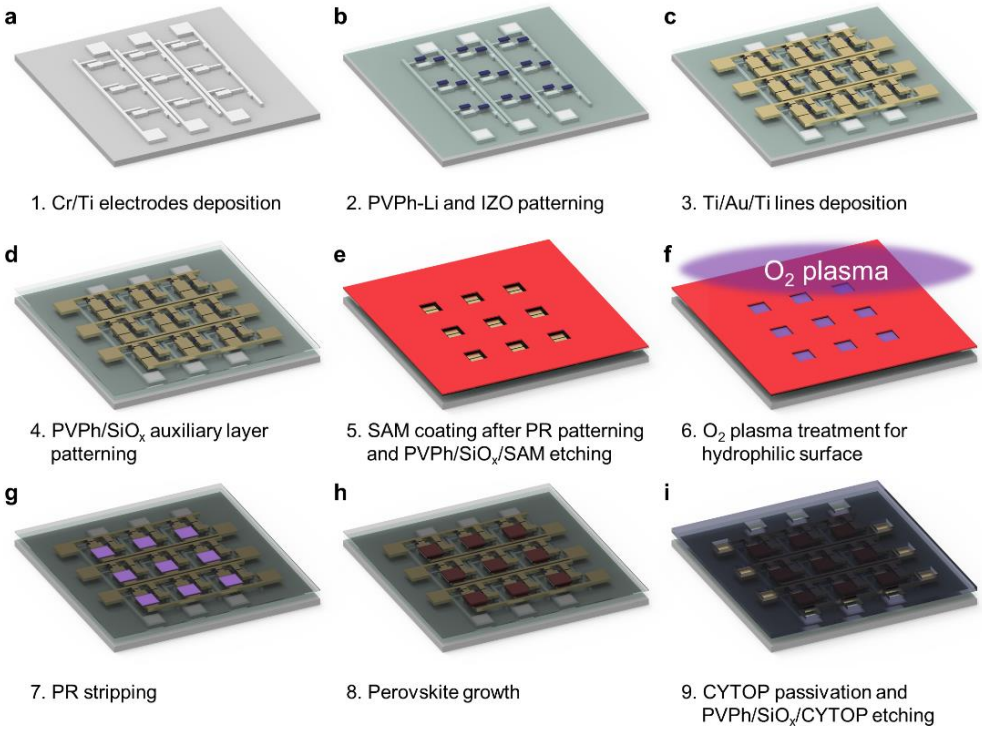

Figure S1. a-i) A fabrication process of the 3 × 3 DAVAN device array for emulating a visual nervous system.

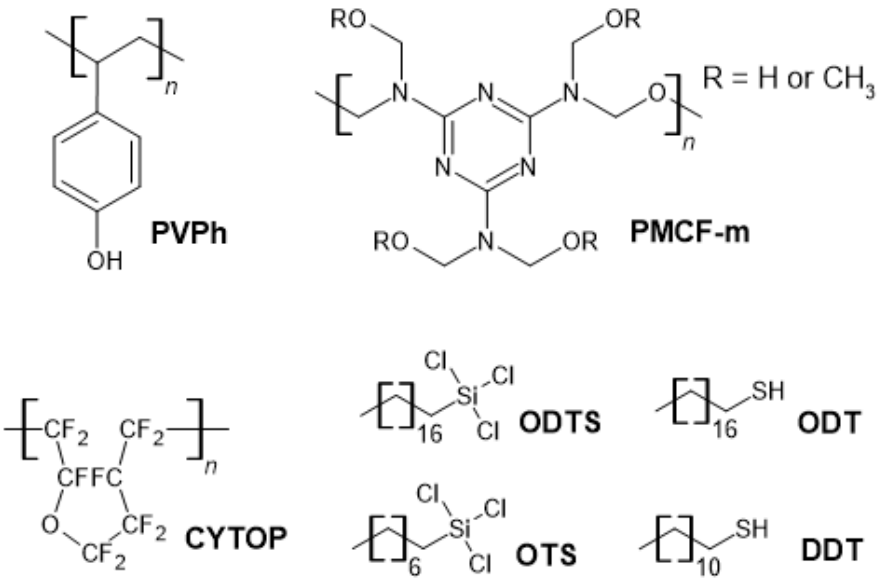

Figure S2. Molecular structure of poly(4-vinylphenol) (PVPh), poly(melamine-co-formaldehyde) methylated (PMCF-m), CYTOP, octadecyltrichlorosilane (ODTS), octyltrichlorosilane (OTS), 1-octadecanethiol (ODT), and 1-dodecanethiol (DDT).

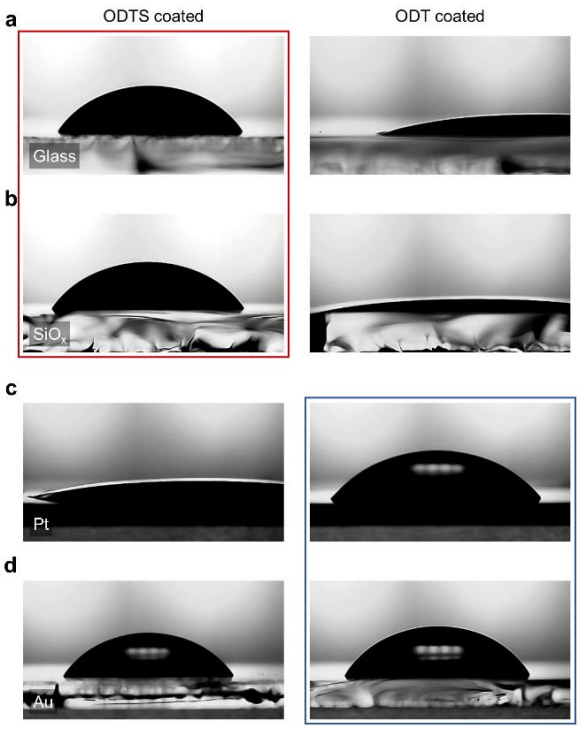

Figure S3. Photograph images of the contact angles of DMF on various surfaces treated by ODTS and ODT. a) glass, b) SiO_x film on glass, c) Pt film on glass, and d) Au film on glass. The measured contact angles are described in Table S1.

a glass

Contact angle (º)	ODTS	OTS	ODT	DDT
DI	108.3 ± 1.8	13.3 ± 1.2	35.9 ± 2.1	25.1 ± 2.0
DMF	59.2 ± 2.7	54.5 ± 1.7	19.4 ± 1.5	9.4 ± 0.7

b SiO_x film on glass

Contact angle (º)	ODTS	OTS	ODT	DDT
DI	109.0 ± 1.2	107.9 ± 0.6	25.8 ± 2.2	20.6 ± 0.8
DMF	57.6 ± 1.5	52.3 ± 1.5	13.4 ± 0.6	11.6 ± 1.4

c Pt film on glass

Contact angle (º)	ODTS	OTS	ODT	DDT
DI	81.4 ± 1.2	81.4 ± 1.2	105.0 ± 0.9	94.4 ± 1.6
DMF	12.3 ± 1.3	14.7 ± 0.9	49.3 ± 2.7	32.4 ± 1.7

d Au film on glass

Contact angle (º)	ODTS	OTS	ODT	DDT
DI	94.1 ± 3.0	88.2 ± 3.5	106.9 ± 0.8	104.9 ± 1.1
DMF	54.1 ± 1.4	29.4 ± 2.7	57.4 ± 1.6	56.3 ± 1.7

Table S1. Measured contact angles of DI and DMF on various surfaces treated by ODTS, OTS, ODT, and DDT. a) glass, b) SiO_x film on glass, c) Pt film on glass, and d) Au film on glass.

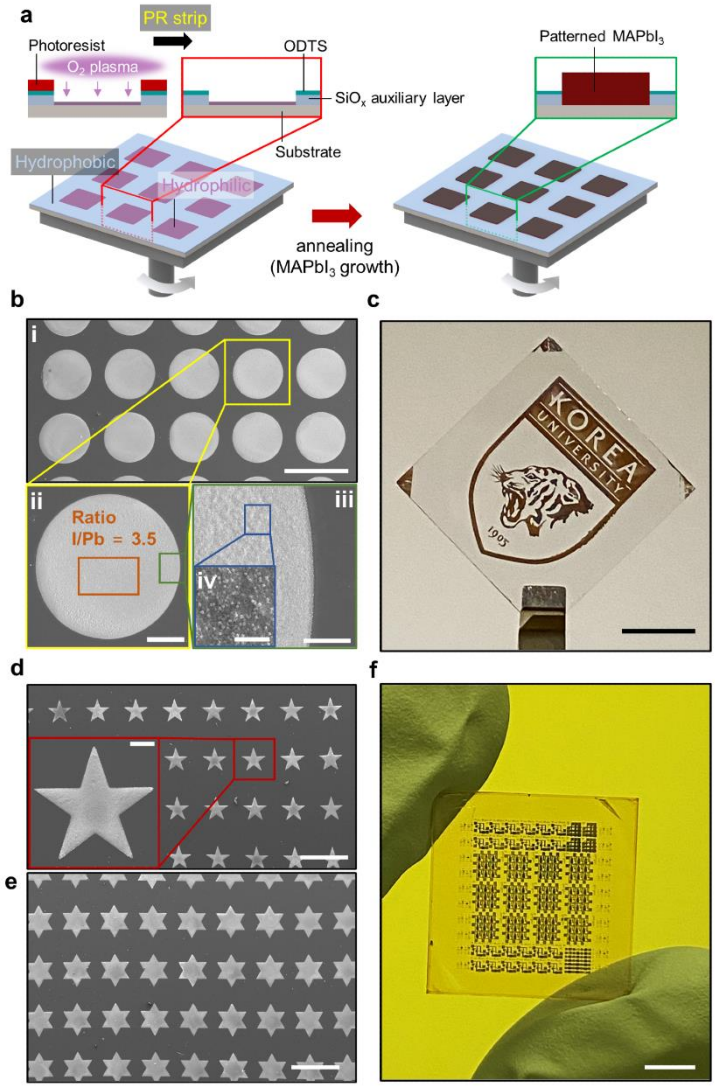

Figure S4. a) A synthesis process of perovskite arrays on a hydrophilic/hydrophobic treated substrate using spin-coating. b) i) SEM image of circularly patterned $MAPbI_3$ arrays on SiO_x-assisted glass substrate (scale bar: 500 μm), ii) its magnified SEM image and EDS map (scale bar: 100 μm), iii) SEM image of edge side of film (scale bar: 20 μm), and iv) another magnified SEM image (scale bar: 2 μm). c) Photograph image of a sophisticatly patterned $MAPbI_3$ film (scale bar: 10 mm). d) i) SEM image of stellately patterned $MAPbI_3$ arrays (scale bar: 500 μm) and ii) its magnified SEM image (scale bar: 50 μm). e) Another shaped SEM image of patterned $MAPbI_3$ arrays (scale bar: 500 μm). f) Photograph image of fully processed DAVAN arrays on glass substrate of dimensions 2 cm × 2 cm (scale bar: 5 mm).

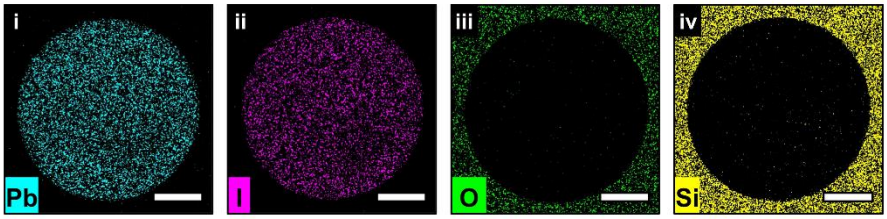

Figure S5. EDS maps of i) Pb, ii) I, iii) O, and iv) Si obtained from the circularly patterned $MAPbI_3$ film (scale bar: 100 μm).

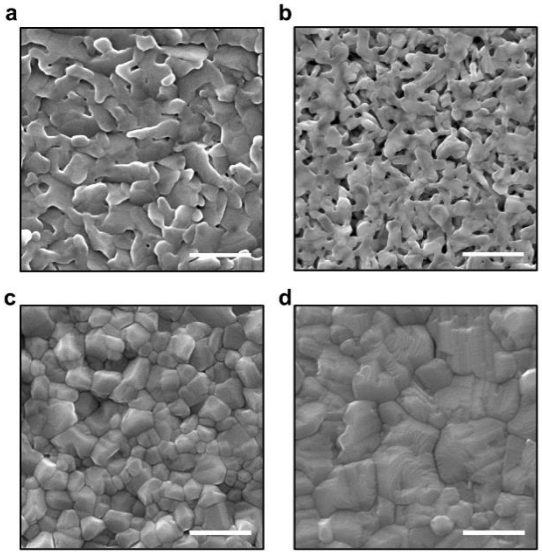

Figure S6. SEM images of as-synthesized a) c-PbI_2 film, b) p-PbI_2 film, c) $MAPbI_3$ film from c-PbI_2, and d) $MAPbI_3$ film from p-PbI_2. All scale bars denote 1 μm. For comparison, c-PbI_2 films was prepared by a conventional annealing method. In other words, the as-spin-coated PbI_2 films were annealed at 90 °C for 5 min instead of being immersed in IPA. A compact morphology of $MAPbI_3$ film was obtained by using anti-solvent extraction method.

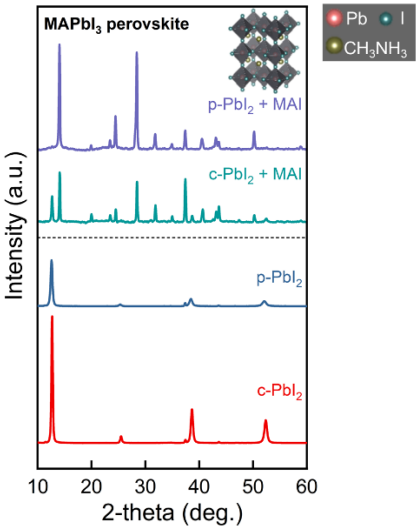

Figure S7. XRD profiles of $MAPbI_3$ and PbI_2 films on glass prepared by conventional annealing method (c-PbI_2 + MAI) and anti-solvent extraction method (p-PbI_2 + MAI).

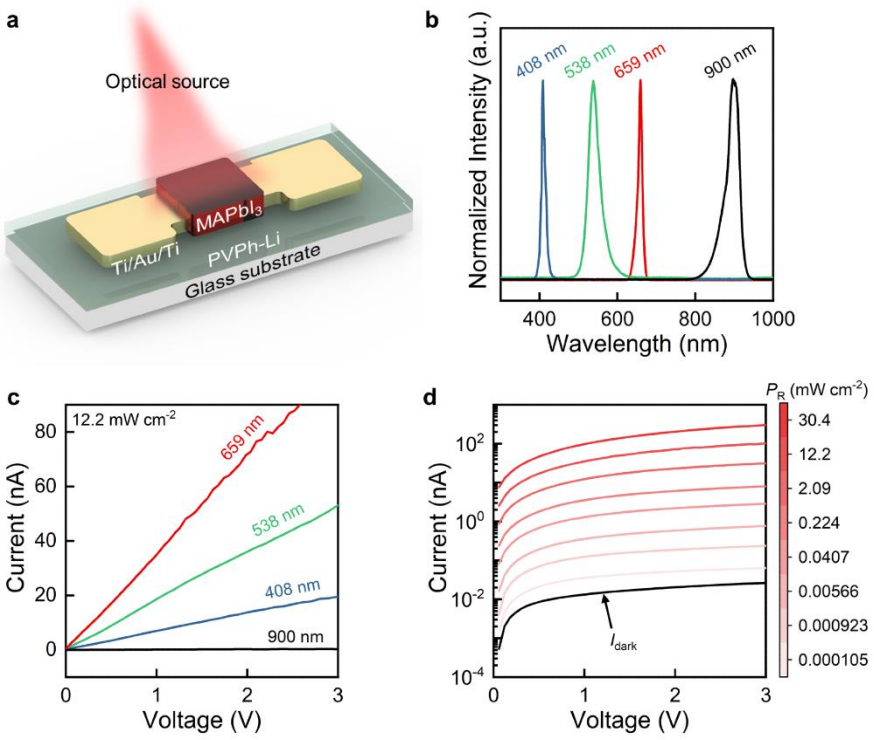

Figure S8. a) Schematic illustration of $MAPbI_3$ PD. b) Emission spectra of 408, 538, 659, and 900 nm laser diodes. c) *I–V* curves of the $MAPbI_3$ PD under light irradiation (12.2 mW cm^{-2}) with different wavelengths. d) *I–V* curves of the $MAPbI_3$ PD under different optical power densities under a bias voltage of 3 V.

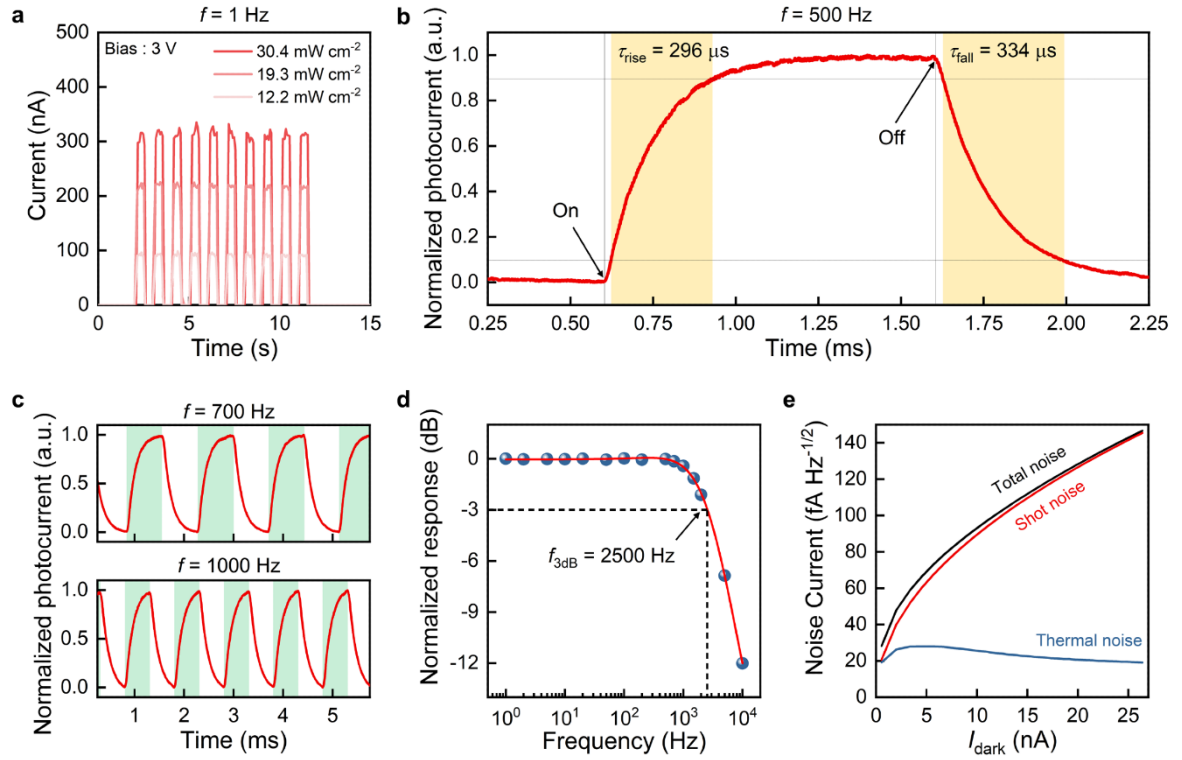

Figure S9. a) Photoresponse of the $MAPbI_3$ PD under different P_R at 3 V bias. High-frequency photoresponse of the $MAPbI_3$ PD under P_R of 30.4 mW cm^{-2} with b) 500, and c) 700 and 1000 Hz. d) 3 dB bandwidth of the $MAPbI_3$ PD at 3 V bias. e) The plot of calculated noise current versus I_{dark} of the $MAPbI_3$ PD. Two noise currents, shot noise and thermal noise, are the main contributor to I_{dark} which fluctuates randomly. The total noise current can be expressed as $I_{\text{total noise}} = \sqrt{I_{\text{shot noise}}{}^2 + I_{\text{thermal noise}}{}^2}$. When the $MAPbI_3$ PD is operated at 3 V bias, the thermal noise is much lower than the shot noise. In this study, the thermal noise can be negligible and the detectivity of the device can be limited by the larger shot noise.

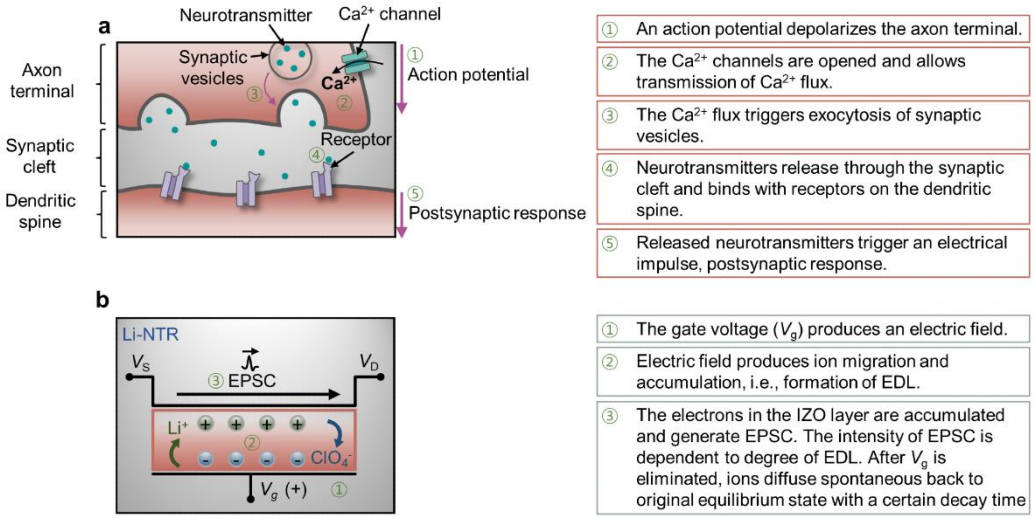

Figure S10. a) An overview of electrical information transmission process from presynaptic neuron to postsynaptic neuron. b) An overview of the operating mechanism of Li-NTR similar to the biological synaptic information transmission process.

Synaptic device structure	Sensory elements	Sensory modality	Adaptation functionality	Stimulus pulse width	Adaptation decay constant[a)]	Energy consumption with/ without adaptation[b)]	Ref.
TiN/Ti/HfO_x/W	–	–	Yes	10–100 ms	20–40 ms	–	[S5]
Pt/LLTO/Pt	–	–	Yes	0.4 s	–	–	[S6]
ITO/PVA:$CaCl_2$	CNT-coated PDMS pressure sensor and $PEA_2MA_2Pb_3I_{10}$ photodetector	Pressure and Light	–	1–10 s	–	–	[S7]
$CsPb(Br_{0.5}I_{0.5})_3$ /MoS_2	$CsPb(Br_{0.5}I_{0.5})_3$	Light	Yes	0.5 s	–	–	[S8]
TiN/Li_xSiO_y/Pt	–	–	Yes	0.1–700 μs	–	100 μJ/ 206 μJ in 80 ms (pulse period of 3 ms, pulse width of 700 μs, and voltage bias of 3.2 V)	[S9]
Pentacene/PMMA/NT-CN	NT-CN	Light	–	20–2000 ms and DC	–	–	[S10]
IGZO/SAO	CdSe photosensor	Light	Yes	0.5 s	–	–	[S11]
PTCDI-C_8/CuPc/PTCDI-C_8	PTCDI-C_8/ CuPc/PTCDI-C_8	Oxygen	–	0.1–0.4 s	–	–	[S12]
PTCDA/MoS_2	PTCDA	Light	–	25–400 ms	–	–	[S13]
$CsPbBr_3$/MoS_2	$CsPbBr_3$	Light	Yes	0.04–4 s	–	1 μJ/ 1.7 μJ in 5 s (38 mW cm^{-2} and gate bias of 15 V)	[S14]
PDPP3T/PVCN/PVA/ PBTTT/PVCN	–	–	Yes	4 s	0.06–4 s	0.1 μJ/ 3.5 μJ in 5 s (fast adaptation device with gate bias of −6 V)	[S15]
In_2O_3/AlLiO	–	–	–	30–200 ms	–	–	[S16]
MoS_2/ (PEGDA:HOMPP:[EMIM][TFSI])	PTFE pressure sensor	Pressure	–	0.08–1.75 s	–	–	[S17]
ZnO/PVPh	–	–	–	0.1–5 s	–	–	[S18]
Au/Nafion/ITO	PDMS pressure sensor	Pressure	–	0.1–0.5 s	–	–	[S19]
Nafion/WO_3	–	–	–	5 ms	–	–	[S20]
rGO/PEO:$LiClO_4$	–	–	–	40–187 ms	–	–	[S21]
PDPP3T:PCBM/PVCN/PVA/ PBTTT:PCBM /PVCN	PDPP3T:PCBM	Light	Yes	few second	0.2–1000 s	0.40 μJ/ 3.07 μJ in 5 s (1 × 10^6 cd m^{-2})	[S22]
IZO/PVPh-Li	$MAPbI_3$ photodetector	Light	Yes	0.5 s	3–329 s	135 μJ/ 700 μJ in 50 s (P_R of 30.4 mW cm^{-2} and V_{LWC} of 1 V)	This work

[a)]The adaptation decay constant is quantified by fitting the exponential decay model. [b)]The devices display various transient current responses, where the comparable energy consumptions of with/without adaptation are selected.

Table S2. Comparison of the proposed synaptic device and previously reported results.

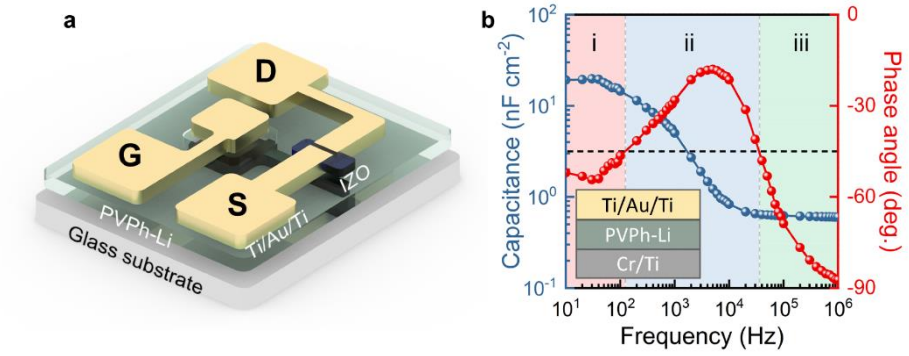

Figure S11. a) Schematic illustration of Li-NTR. The gate electrode near the IZO channel consisted of Cr/Ti stacked film and connected by Ti/Au/Ti pad for characterization. b) Frequency-dependent capacitance and phase angle curves for a PVPh-Li based MOM capacitor. The ionic polarization can be classified with a capacitive ($|\theta| > 45°$) or resistive ($|\theta| < 45°$) behavior. Three different frequency regions can be clearly divided: i) at low frequencies ($f < 2 \times 10^2$ Hz, $|\theta| > 45°$), the formation of EDL in the PVPh-Li electrolyte is dominant for the capacitive behavior; ii) at medium frequencies (2×10^2 Hz $< f < 4 \times 10^4$ Hz, $|\theta| < 45°$), the ion relaxation or ion migration is dominant for the resistive behavior; at high frequencies ($f > 4 \times 10^4$ Hz, $|\theta| > 45°$), the dipolar relaxation of the PVPh-Li electrolyte is dominant for the capacitive behavior.

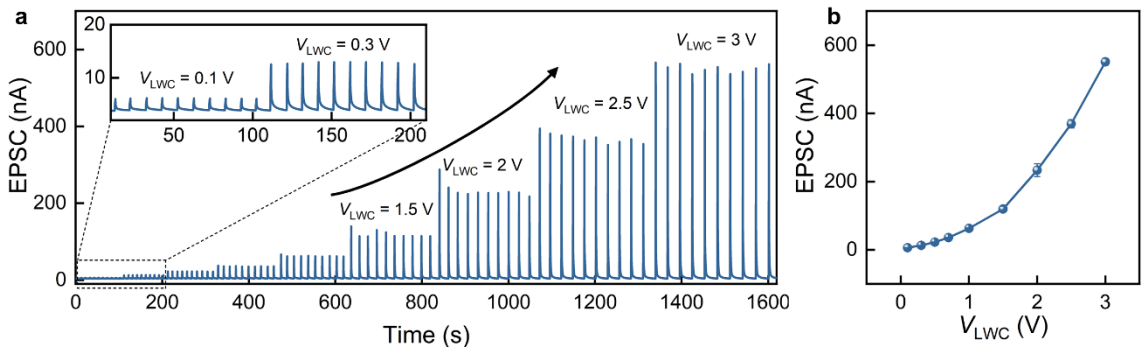

Figure S12. a) The EPSC responses under ten V_{LWC} with different pulse amplitudes (PW = 0.5 s). b) The plot of $EPSC_{peak}$ as a function of V_{LWC} amplitude.

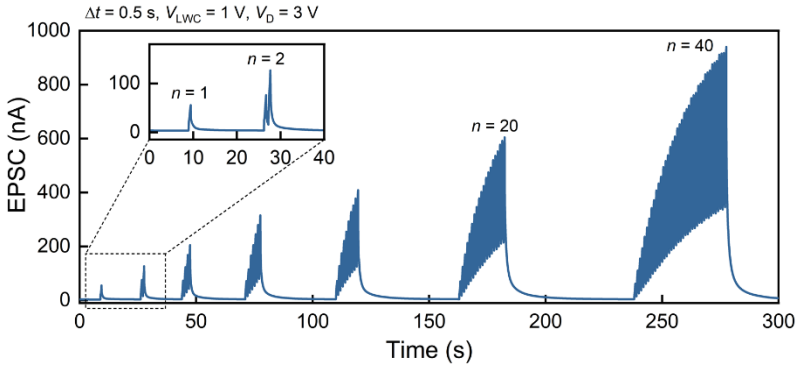

Figure S13. a) The EPSC responses to multiple V_{LWC} (1 V, 1 Hz). The inset is the EPSC response under n = 1 and n = 2.

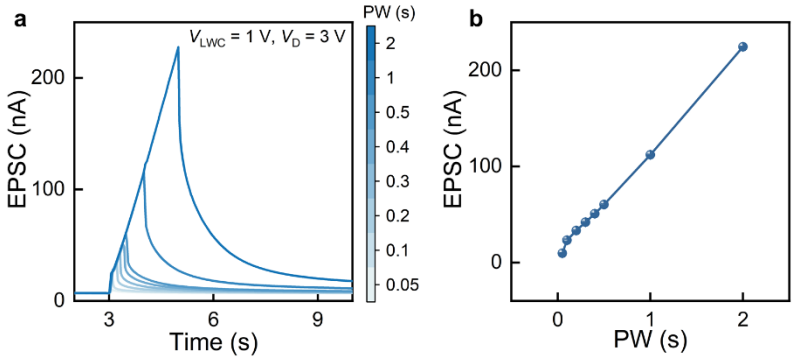

Figure S14. a) The EPSC responses to single V_{LWC} with different PWs. b) The plot of $EPSC_{peak}$ as a function of PW.

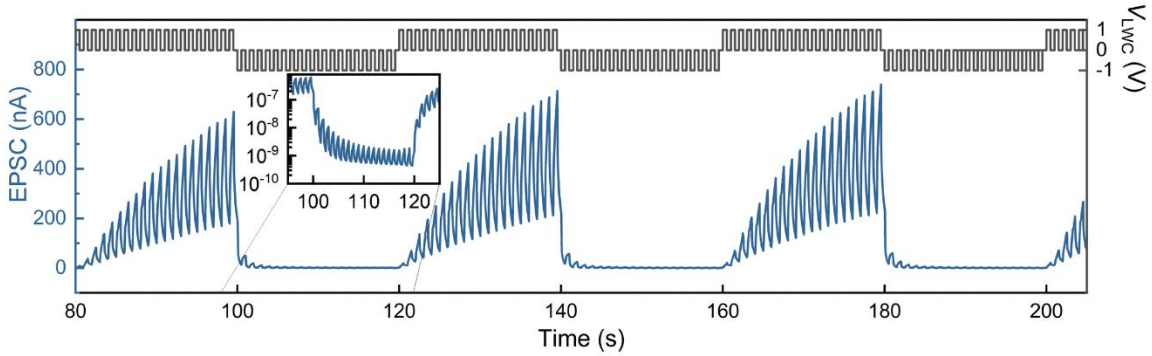

Figure S15. a) The EPSC responses of the Li-NTR by applying 20 positive and 20 negative V_{LWC}s with an amplitude of 1 V and − 1 V.

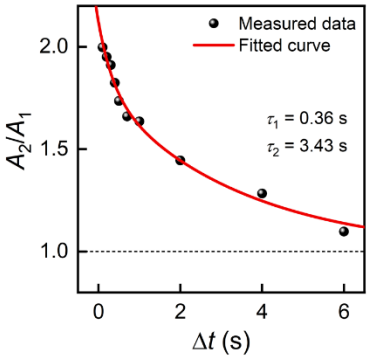

Figure S16. Dependence of PPF index (A_2/A_1) on pulse delay (Δt). The A_2/A_1 decreases with increasing Δt in a simple double-exponential decay model, indicating that the present results are comparable to the biological synaptic plasticity.

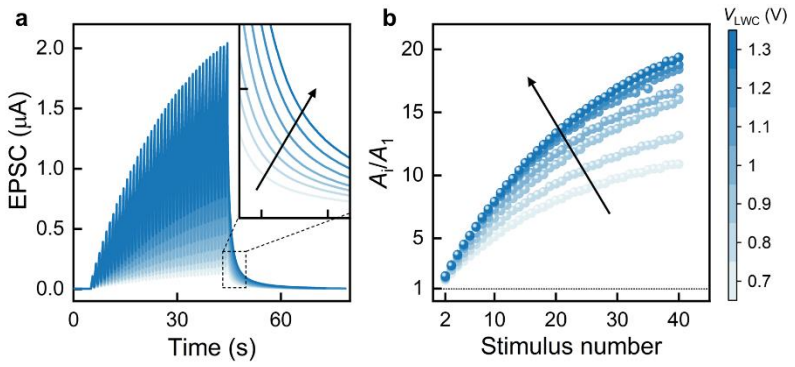

Figure S17. a) The EPSC responses under 40 V_{LWC} with different pulse amplitudes. The inset is an enlarged view of the EPSC response under decaying. b) The plot of A_i/A_1 vs. stimulus number for V_{LWC}. The A_i/A_1 increases with increasing stimulus number and V_{LWC}.

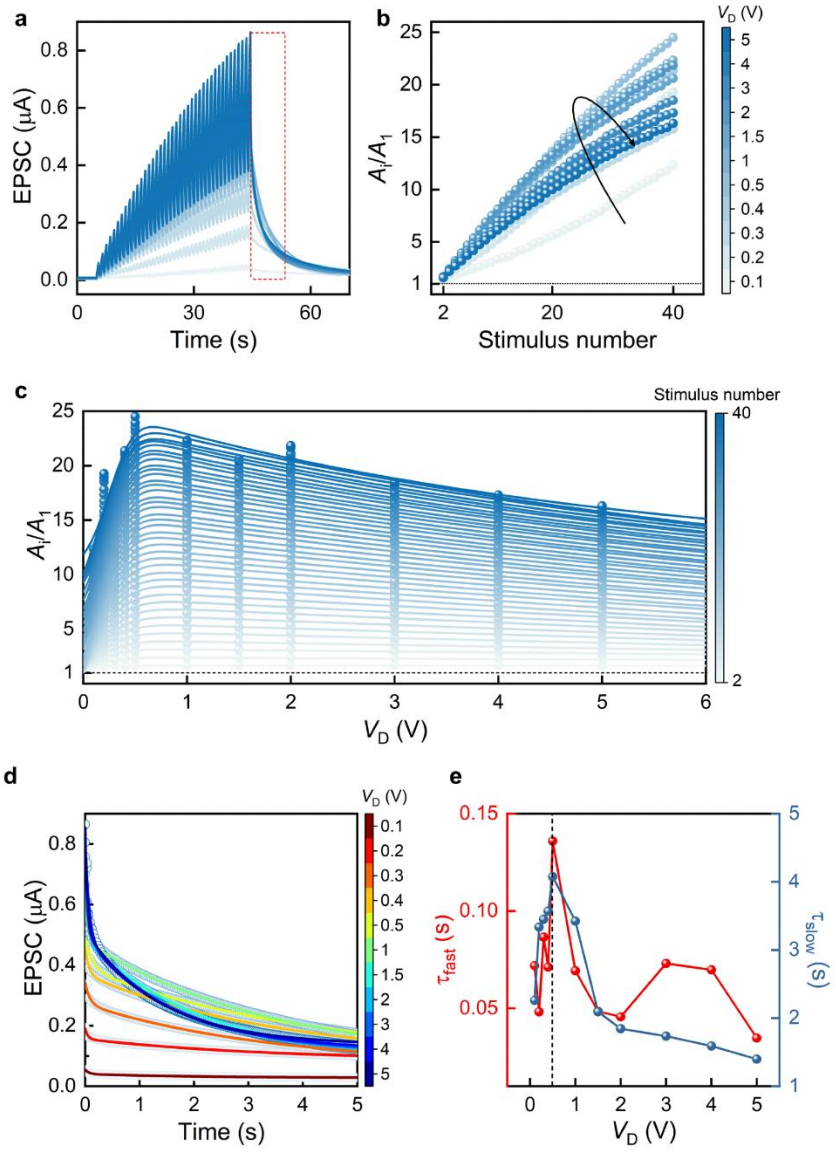

Figure S18. a) The EPSC responses under 40 V_{LWC} with different V_D. b) The plots of A_i/A_1 vs. stimulus number for V_D. The increasing trend of A_i/A_1 increases with increasing stimulus number and V_D until V_D of 0.5 V, but steadily decreases with further increase in V_D. c) The plots of A_i/A_1 vs. V_D for stimulus number. d) The enlarged view of decaying behavior of EPSC responses in a) and corresponding fitting curves with double-exponential model. e) The plots of τ_{fast} and τ_{slow} as a function of V_D. These results indicate that the facilitation and the decay properties of Li-NTR are influenced by V_D. Applying a high V_D can generate large in-plane electric fields in the IZO layer, providing a large driving force for extracting the trapped charges at the PVPh-Li/IZO interface. This large driving force causes the fast EPSC decay.

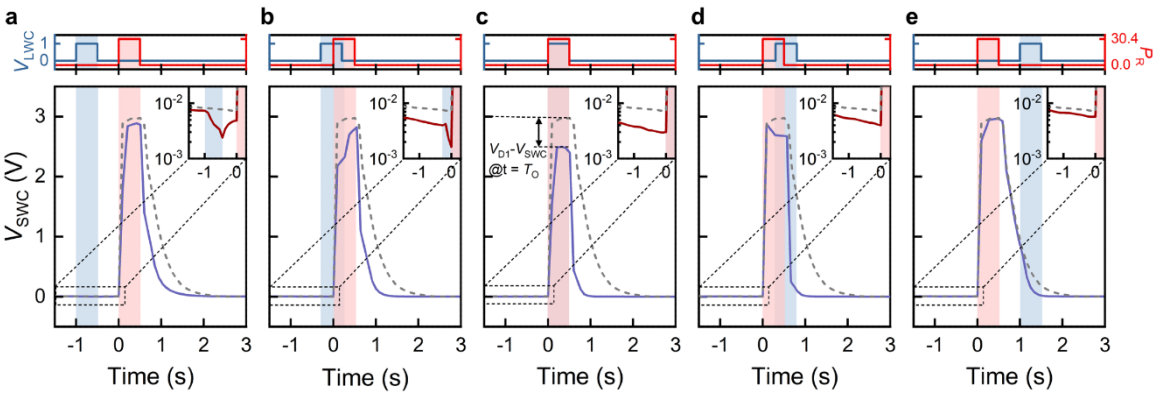

Figure S19. Transient changes of V_{SWC} at ΔT are a) – 1 s, b) – 0.3 s, c) 0 s, d) 0.3 s, and e) 1 s, the peak values of V_{SWC} are obtained at ΔT = 0 s. These results indicate that the V_{SWC} responses are completely related to V_{LWC}.

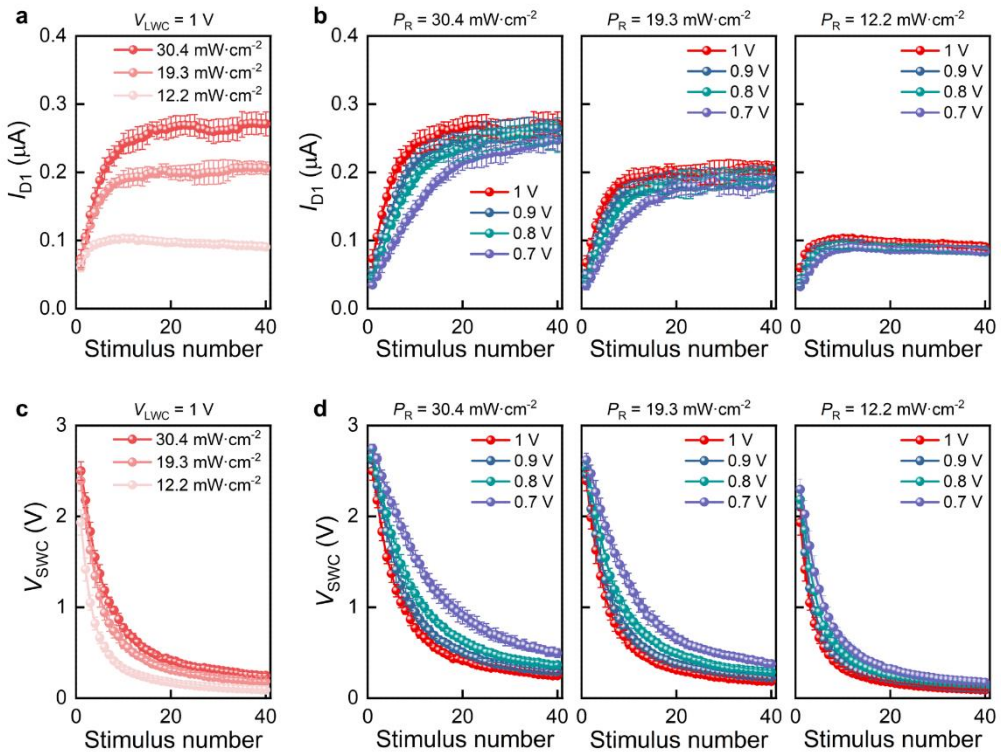

Figure S20. The peak values of I_{D1} vs. stimulus number are plotted a) under V_{LWC} of 1 V as a function of P_R. The peak values of I_{D1} are plotted b) under P_R of 30.4 mW cm^{-2} (left), 19.3 mW cm^{-2} (middle), and 12.2 mW cm^{-2} (right) with different V_{LWC}. The peak values of V_{SWC} vs. stimulus number are plotted a) under V_{LWC} of 1 V as a function of P_R and The peak values of V_{SWC} are plotted b) under P_R of 30.4 mW cm^{-2} (left), 19.3 mW cm^{-2} (middle), and 12.2 mW cm^{-2} (right) with different V_{LWC}.

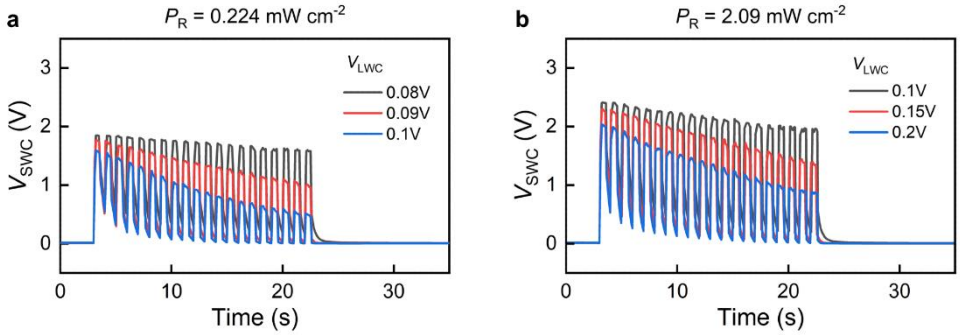

Figure S21. Dynamic V_{SWC} responses of the artificial photoreceptor under 20 optical stimuli a) 0.224 and b) 2.09 mW cm^{-2} with various V_{LWC}. Both pulsed optical and electrical stimuli are applied at the same period of 1 s and PW of 0.5 s.

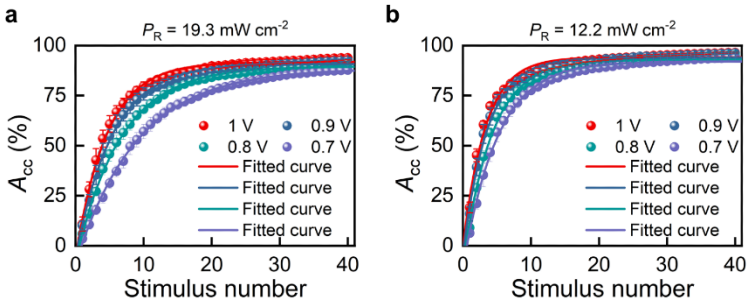

Figure S22. The accuracies vs. stimulus number are plotted under fixed P_R of a) 19.3 mW cm^{-2} and b) 12.2 mW cm^{-2} as a function of V_{LWC}.

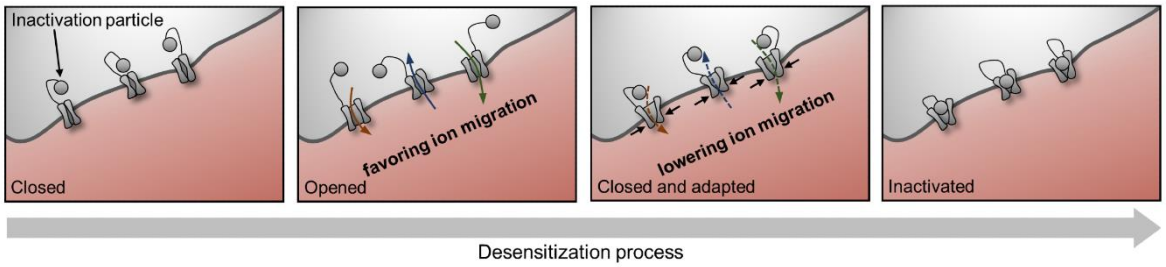

Figure S23. Schematic illustrations of the model for the desensitization process of mechanotransducer channels in a sensory neuron.

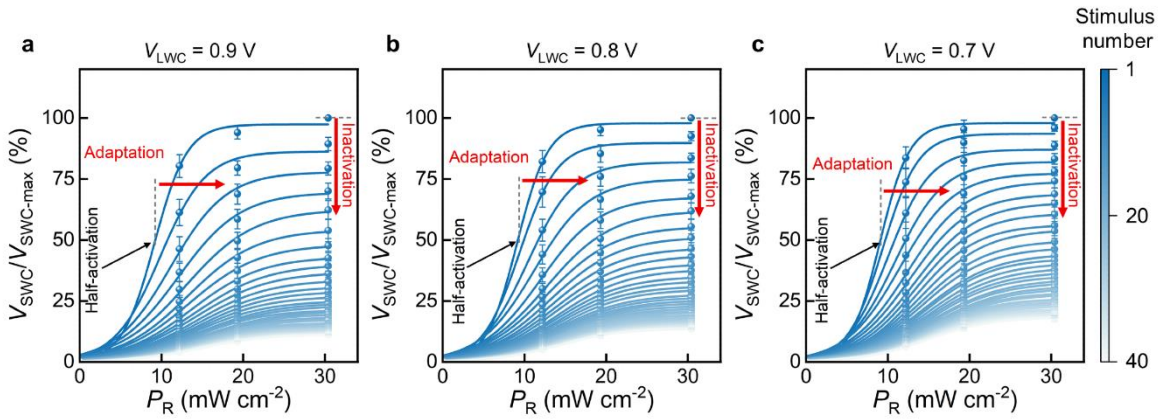

Figure S24. The normalized V_{SWC} vs. P_R are plotted under fixed V_{LWC} of a) 0.9 V, b) 0.8 V, and c) 0.7 V as a function of stimulus number.

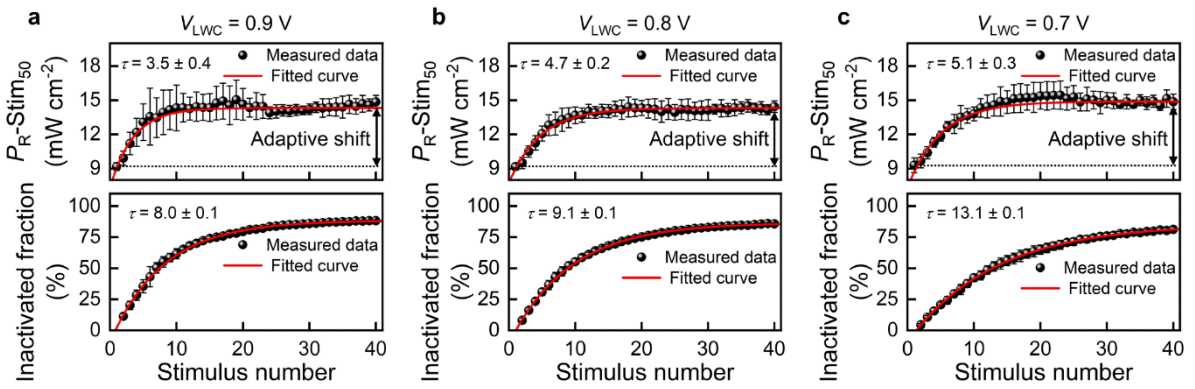

Figure S25. The calculated $Stim_{50}$ and inactivation fraction vs. stimulus number are plotted under fixed V_{LWC} of 0.9 V, b) 0.8 V, and c) 0.7 V as a function of P_R.

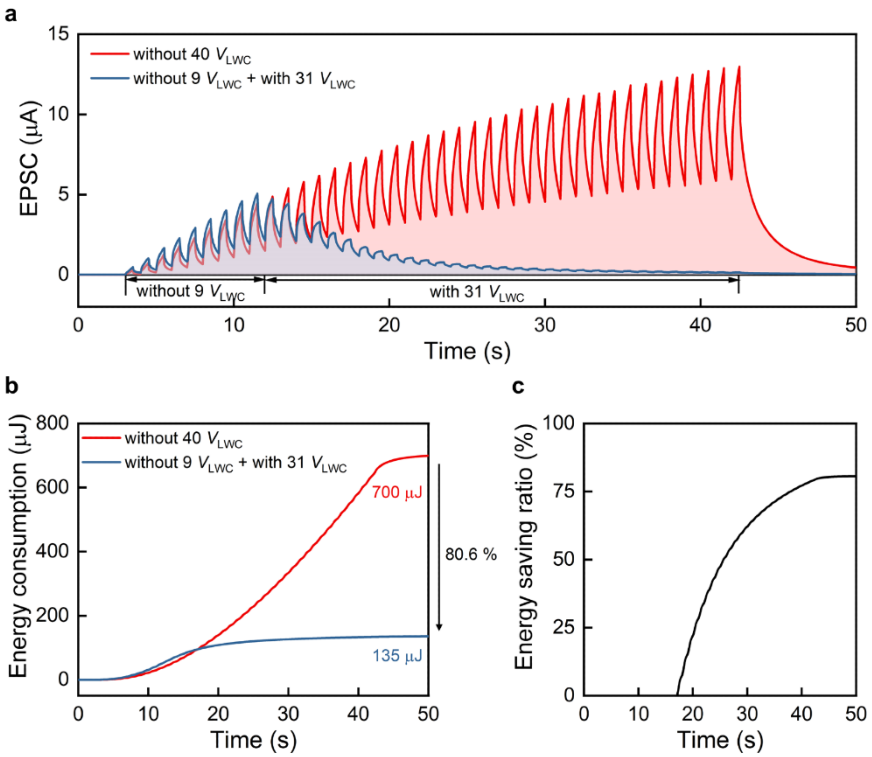

Figure S26. Energy consumption comparison of the DAVAN device. a) Transient EPSC responses of the DAVAN device derived from Figure 4c under repeated optical irradiations without V_{LWC} and the onset of V_{LWC} at the 10$^{\mathrm{th}}$ stimulus. b) The energy consumption comparison and c) energy saving ratio of the DAVAN device with/without V_{LWC}. Here, the energy consumption of the response can be explained by the following equation $E = \int V_{\mathrm{D2}} \times \mathrm{EPSC}\, dt$.

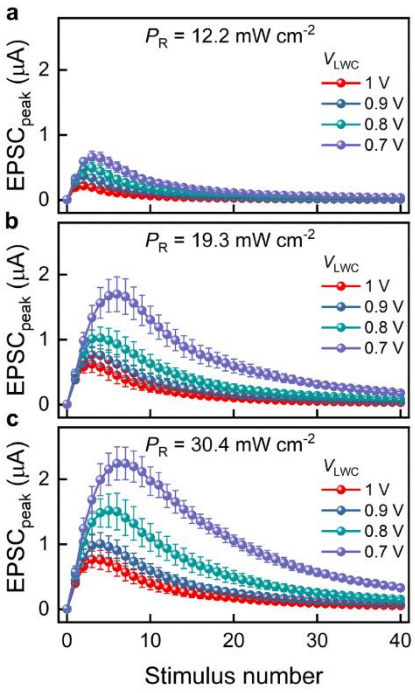

Figure S27. The $EPSC_{peak}$ vs. stimulus number are plotted under fixed P_R of a) 12.2 mW cm^{-2}, b) 19.3 mW cm^{-2}, and c) 30.4 mW cm^{-2} as a function of V_{LWC}.

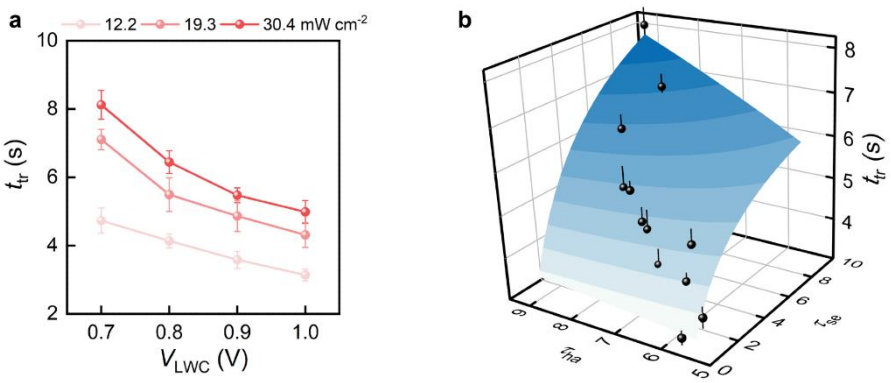

Figure S28. a) The derived t_{tr} vs. V_{LWC} are plotted as a function of P_R. b) 3D plot of t_{tr} as a function of τ_{se} and τ_{ha} and the fitted surface using Equation (S2).

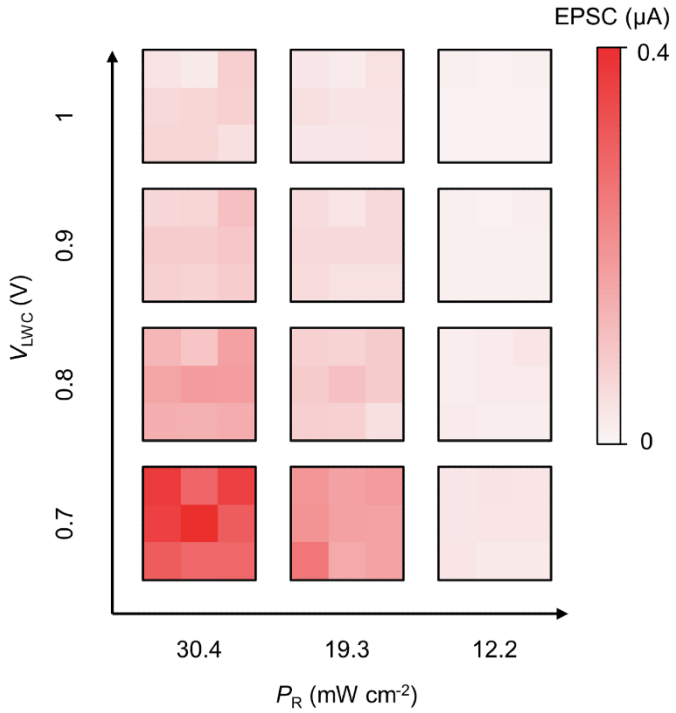

Figure S29. Encoded images of the EPSC of the 3 × 3 DAVAN device array at the 40th stimulus number under various optical (12.2–30.4 mW cm^{-2}) and electrical (0.7–1 V) stimuli. These results indicate that the pixels investigated are functional with satisfactory uniformity.

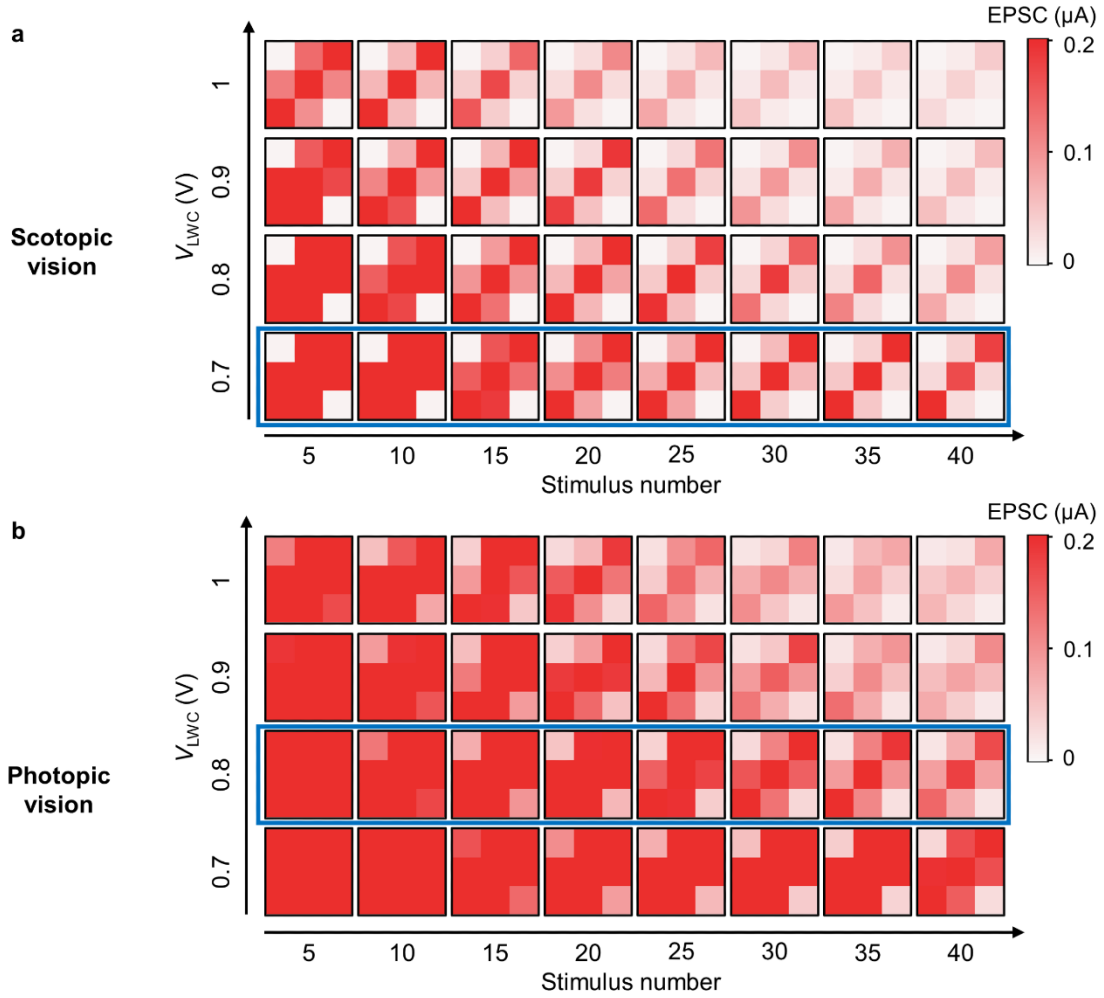

Figure S30. Encoded image sets of the 3 × 3 DAVAN device array under light irradiation with various V_{LWC} such as a) scotopic vision and b) photopic vision.

Reference

[S1] J. Hao, P. Delmas, *J. Neurosci.* **2010**, *30*, 13384.

[S2] J.-Y. Kim, E. K. Lee, J. Jung, D.-W. Lee, Y. Yun, J. W. Chung, J.-I. Park, J.-J. Kim, *J. Mater. Chem. C* **2019**, *7*, 5821.

[S3] W. Lee, J. Lee, H. Yun, J. Kim, J. Park, C. Choi, D. C. Kim, H. Seo, H. Lee, J. W. Yu, W. B. Lee, D.-H. Kim, *Adv. Mater.* **2017**, *29*, 1702902.

[S4] H. Zheng, W. Wang, Y. Liu, J. Sun, *J. Power Sources* **2017**, *344*, 46.

[S5] X. Yang, Y. Fang, Z. Yu, Z. Wang, T. Zhang, M. Yin, M. Lin, Y. Yang, Y. Cai, R. Huang, *Nanoscale* **2016**, *8*, 18897.

[S6] T. Shi, J. F. Wu, Y. Liu, R. Yang, X. Guo, *Adv. Electron. Mater.* **2017**, *3*, 1700046.

[S7] C. Wan, P. Cai, X. Guo, M. Wang, N. Matsuhisa, L. Yang, Z. Lv, Y. Luo, X. J. Loh, X. Chen, *Nat. Commun.* **2020**, *11*, 1.

[S8] S. Hong, S. H. Choi, J. Park, H. Yoo, J. Y. Oh, E. Hwang, D. H. Yoon, S. Kim, *ACS Nano* **2020**, *14*, 9796.

[S9] Z. Wu, J. Lu, T. Shi, X. Zhao, X. Zhang, Y. Yang, F. Wu, Y. Li, Q. Liu, M. Liu, *Adv. Mater.* **2020**, *32*, 2004398.

[S10] H. L. Park, H. Kim, D. Lim, H. Zhou, Y. H. Kim, Y. Lee, S. Park, T. W. Lee, *Adv. Mater.* **2020**, *32*, 1906899.

[S11] S. M. Kwon, S. W. Cho, M. Kim, J. S. Heo, Y. H. Kim, S. K. Park, *Adv. Mater.* **2019**, *31*, 1906433.

[S12] C. Qian, Y. Choi, Y. J. Choi, S. Kim, Y. Y. Choi, D. G. Roe, M. S. Kang, J. Sun, J. H. Cho, *Adv. Mater.* **2020**, *32*, 2002653.

[S13] S. Wang, C. Chen, Z. Yu, Y. He, X. Chen, Q. Wan, Y. Shi, D. W. Zhang, H. Zhou, X. Wang, P. Zhou, *Adv. Mater.* **2019**, *31*, 1806227.

[S14] D. Xie, L. Wei, M. Xie, L. Jiang, J. Yang, J. He, J. Jiang, *Adv. Funct. Mater.* **2021**, *31*, 2010655.

[S15] H. Shen, Z. He, W. Jin, L. Xiang, W. Zhao, C.-a. Di, D. Zhu, *Adv. Mater.* **2019**, *31*, 1905018.

[S16] J. Li, D. Jiang, Y. Yang, Y. Zhou, Q. Chen, J. Zhang, *Adv. Electron. Mater.* **2020**, *6*, 1901363.

[S17] J. Yu, G. Gao, J. Huang, X. Yang, J. Han, H. Zhang, Y. Chen, C. Zhao, Q. Sun, Z. L. Wang, *Nat. Commun.* **2021**, *12*, 1.

[S18] H. Faber, M. Burkhardt, A. Jedaa, D. Kälblein, H. Klauk, M. Halik, *Adv. Mater.* **2009**, *21*, 3099.

[S19] C. Zhang, W. B. Ye, K. Zhou, H. Y. Chen, J. Q. Yang, G. Ding, X. Chen, Y. Zhou, L. Zhou, F. Li, S.-T. Han, *Adv. Funct. Mater.* **2019**, *29*, 1808783.

[S20] X. Yao, K. Klyukin, W. Lu, M. Onen, S. Ryu, D. Kim, N. Emond, I. Waluyo, A. Hunt, J. A. del Alamo, J. Li, B. Yildiz, *Nat. Commun.* **2020**, *11*, 1.

[S21] M.-J. Park, Y. Park, J.-S. Lee, *ACS Appl. Electron. Mater.* **2020**, *2*, 339.

[S22] Z. He, H. Shen, D. Ye, L. Xiang, W. Zhao, J. Ding, F. Zhang, C.-a. Di, D. Zhu, *Nat. Electron.* **2021**, *4*, 522.